Experimental and numerical investigation of electrohydrodynamic flow in a point-to-ring corona discharge

Yifei Guan, Ravi Sankar Vaddi, Alberto Aliseda, and Igor Novosselov

Phys. Rev. Fluids **3**, 043701 — Published 20 April 2018

DOI: 10.1103/PhysRevFluids.3.043701

Experimental and Numerical Investigation of Electro-Hydrodynamic Flow in a Point-to-Ring Corona Discharge

Yifei Guan, Ravi Sankar Vaddi, Alberto Aliseda and Igor Novosselov [§]

Department of Mechanical Engineering, University of Washington, Seattle, U.S.A. 98195

October 2017

An electrohydrodynamic (EHD) flow in a point-to-ring corona configuration is investigated experimentally and via a novel multiphysics computational model. The model couples the ion transport equation and the Navier-Stokes equations (NSE) to solve for the spatiotemporal distribution of electric field, flow field, and charge density. The numerical simulation results are validated against experimental measurements of the cathode voltage, ion concentration, and velocity profiles. The maximum flow velocity is at the centerline, and it decays rapidly with radial distance due to the viscous and electric forces acting on the partially-ionized gas. To understand this coupling, a new non-dimensional parameter, X, is formulated as the ratio of the local electric force to the inertial term in the NSE. In the region of $\mathrm{X} \geq 1$, the electric force dominates the flow dynamics, while in the X<<1 region, the balance of viscous and inertial terms yields traditional pipe flow characteristics. This approach expands on the analytical model of Guan et al. by adding a description of the developing flow region. The approach allows the model to be used for the entire EHD domain, providing insights into the near-field flow in the corona region.

I. INTRODUCTION

Electrohydrodynamic (EHD) propulsion, also referred to as ionic wind in the literature, has many practical applications, such as convective cooling [1-5], electrostatic precipitators (ESP) [6-9], plasma-assisted combustion [10], airflow control [11], turbulent boundary layer actuators [12], and surface particle trapping [13]. A high voltage corona discharge generates streams of ions between the two electrodes, and the high-velocity ions transfer their kinetic energy to the neutral air molecules outside the corona through collisions, accelerating the gas in the direction of the ion drift. The ions' interaction with the neutral molecules can be modeled as an external force term (Lorentz force) in the Navier-Stokes equations [14,15]. Insights into the multiphysics nature of the EHD flow are important for understanding this phenomenon. To correctly predict the flow established by this force, the following elements need to be considered: (i) the electric field resulting from the potential difference between the corona and ground electrodes, as well as its modifications due to the space charge in the high ion concentration in the region; (ii) the ion motion in the resulting electric field; (iii) the interaction between the ion drift and the neutral gas in the flow acceleration region; (iv) the viscous and turbulent stresses; and (v) the effects of developing complex flow patterns as a result of the accelerating flow and device geometry.

When a high voltage is applied, the neutral air molecules are broken down by the strong electric field near the corona electrode. In a positive corona, the electrons are attracted to the anode; positive ions, such as O_2^+ and O^+ [16-18], drift to the cathode, which generates ionic wind. A quadratic voltage-current $(\varphi - I)$ relation was described by Townsend and validated for a coaxial corona discharge configuration [19,20]. Other corona discharge configurations also follow a quadratic relation with modifications due to specific parameters in the configuration, e.g., point-to-pot [16], point-to-plate [21], point-to-grid [22], sphere-to-plane [23], coaxial cylinders [24,25], wire-cylinder-plate [26], point-to-ring [15,27,28], parallel electrodes [29], multi-electrodes [30], and non-uniform electric fields [31]. Guan et al. [32] developed an analytical model generalizing the $(\varphi - I)$ relationship independent of the corona configuration, which parameterizes one-dimensional flow in the direction

---

[§] ivn@uw.edu

of the electric field gradient. The analytical model describes the relationship between the electrical properties and charge density for planar, cylindrical, and spherical coordinates. The EHD velocity profile is obtained numerically using a Chebyshev spectral method [33,34]; the model results match the experimental data in the acceleration region but overpredicts the velocity in the regions away from the axis of the domain. In the inertial flow region (away from the centerline), the flow develops under the balance between the EHD force, convective flow acceleration, and viscous shear stresses. The description of the transition between the wall-bounded pipe flow and the corona-driven EHD centerline flow requires additional physics that are not captured in the simplified model. We hypothesize that *the results of the analytical model can be improved in the numerical simulation to describe all EHD flow regions: (i) the application of the EHD force in the axial direction neglects the effect of the three-dimensional nature of the electric field (the formation of complex flow patterns can be described by the numerical model); and (ii) in order to capture the pipe flow, an inertial flow region needs to be modeled.*

To gain insight into the developing EHD flow, a novel approach is formulated and implemented in a computational fluid dynamics (CFD) simulation that solves for the coupled flow and electric fields in the presence of corona discharge. State-of-the-art literature evaluates several corona configurations [35-37]. Numerical modeling has been applied to the design and analysis of electrostatic precipitators (ESP) [38-41] and heat transfer enhancement [1-5]. Previous EHD flow models use an iterative approach to: (i) calculate the electric field and electric force under Kaptzov's hypothesis [42] or Peek's law [43], and (ii) set a constant space charge on the anode so that the solution matches the cathode current from the experimental data. This method requires multiple iterations and is therefore inefficient. In contrast, our modeling approach solves for charge density by introducing a volumetric charge flux derived from the anode current directly. The charge flux is imposed on a "numerical ionization region" determined by the electric field and the thresholds for the onset of ionization. The ionization (charge flux) and spatial charge density are two-way coupled to the NSE solver, avoiding the iterative procedure for solving the electric field. The electric force acts on a volume of fluid, inducing the EHD flow; this ion - bulk flow coupling is similar to the previous work [1-5,35-41].

In this manuscript, we demonstrate a novel numerical approach for EHD flow in a finite volume solver for axisymmetric point-to-ring corona configurations. CFD simulations are used to resolve the spatiotemporal characteristics of the flow, electric fields, and the charge density. The non-dimensional analysis provides insight into the dominant terms in the different EHD flow regions. The electric to kinetic energy transfer efficiency is evaluated for both the model and the experiments.

II. EXPERIMENTAL SETUP

The EHD flow is studied in a point-to-ring internal pipe geometry. FIG. 1 shows the experimental setup. The apparatus consists of a high voltage corona needle and a grounded ring electrode. The anode needle is a 0.5 mm thick tungsten needle with a radius of curvature of 1 μm at the tip (measured using optical microscopy). The sharpness of the needle is important because it affects the corona discharge at lower voltages [44]. The tip of the needle is checked regularly for visible defects to ensure that it does not degrade over time. The ground electrode is a 1.58 mm thick solid solder with an inner radius of 10 mm. The enclosure is fabricated using 3D printing in Polylactic Acid (PLA) polymer. The distance between the anode and cathode (L) is set in the range of 3 mm to 7 mm using spacers. A variable high voltage power supply (Bertan 205B-20R) is used to set the electric potential between the electrodes. The cathode current is measured on the cathode based on a voltage drop across a 1 MΩ resistor.

The EHD experiment is operated in the positive corona mode in a temperature range of 22-25 ^{0}C, a relative humidity of 23-25%, and ambient pressure. For each anode-cathode distance, the voltage is increased from 4 kV (when the outlet velocity is measurable) to ~10 kV (when the arc discharge occurs). Constant current hot-wire anemometry is used to measure the flow velocity profile. A TSI 1213-20 probe connected to the anemometer (AA – 1005) is positioned at the outlet of the device. The anemometer is calibrated for a range of velocities from 0.2 m/s to 8 m/s [45]. The entire experimental setup is mounted on an optical table; the anemometer probe is attached to a three-dimensional translation stage to obtain space-resolved measurements. The data from the anemometer is collected at a frequency of 10 kHz using data acquisition hardware (myRIO-1900) over a sampling time of 30 seconds. The ion concentration at the exit of the device is measured at a distance of 25.4 mm from the outlet using an air ion counter (AIC by Alpha Lab). The ion concentration measurements are not used in the analysis; rather, they provide an order of magnitude comparison between the experiments and simulations. Each experimental condition is tested at least five times to obtain independent statistical samples.

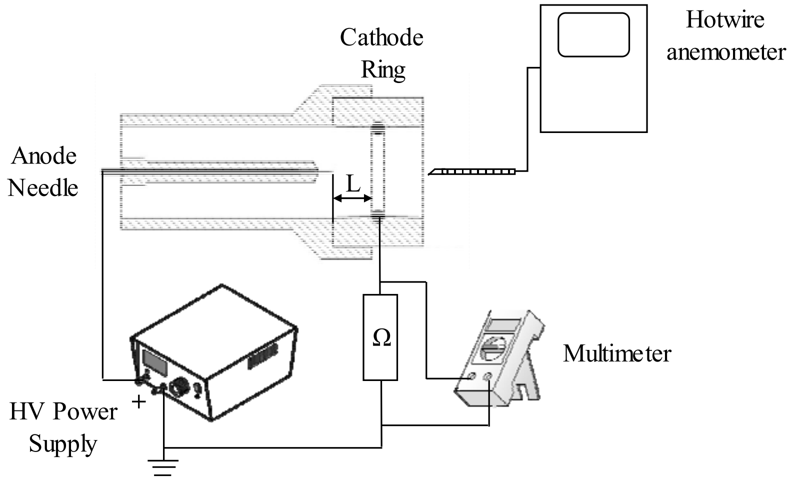

FIG. 1. Schematic of the experimental setup – a high voltage is applied between the corona anode needle and the ion collecting cathode ring. The distance and voltage are varied.

III. NUMERICAL MODELING

A. Governing Equations

The effect of the ion motion interaction on the bulk flow is modeled by adding a body force (electric force) $\mathbf{F_e} = -\rho_e \nabla \varphi$ to the momentum equations. The governing equations used to model the flow are:

$$\nabla \cdot \mathbf{u} = 0 \tag{1}$$

$$\rho \frac{D\mathbf{u}}{Dt} = -\nabla P + \mu \nabla^2 \mathbf{u} - \rho_e \nabla \varphi \ , \tag{2}$$

where ρ, the air density ($1.205\ \text{kg/m}^3$), and μ, the air dynamic viscosity ($1.846\times10^{-5}\ \text{kg/(ms)}$), are constant for incompressible isothermal flow, $\mathbf{u} = \left(u_{\text{axial}}, u_{\text{radial}}\right)$ is the velocity vector in the two-dimensional axisymmetric model, and P is the static pressure. The ion transport is described by the charge density equation:

$$\frac{\partial \rho_e}{\partial t} + \nabla \cdot \left[\left(\mathbf{u} - \mu_b \nabla \varphi \right) \rho_e + D_e \nabla \rho_e \right] = S_e \, . \tag{3}$$

The electric potential is solved using Gauss' law:

$$\nabla^2 \varphi = -\frac{\rho_e}{\varepsilon_0} , \tag{4}$$

where μ_b is the ion mobility, which is approximated as a constant ($2.0\times10^{-4}\ \text{m}^2/(\text{Vs})$) at standard pressure and temperature [21,46], and ε_0 ($\sim 8.854\times10^{-12}\ \text{C/(Vm)}$) is the electric permittivity of free space. Since the relative permittivity of air is close to unity (~1.00059) [47], vacuum permittivity is used in all simulations. D_e is the ion diffusivity described by the electrical mobility equation (Einstein's relation) [32]:

$$D_e = \frac{\mu_b k_B T}{q}, \tag{5}$$

where k_B is Boltzmann's constant ($\sim 1.381 \times 10^{-23}$ J/K), T is the absolute temperature, and q is the electrical charge of an ion, which is equal to the elementary charge (1.602×10^{-19} C).

Ionization is modeled by a volumetric charge flux applied to the fluid within a numerical ionization zone. Instead of defining a surface within the computational domain to model the ionization zone boundary, the volume of the ionization zone is calculated based on the electric field strength computed in the simulation. In Eq. 3, S_e is the volumetric flux term for charge density with the units of $\mathrm{C/(m^3 s)}$:

$$S_e = \begin{cases} I/\Psi, \text{ for } |\mathbf{E}| \in [E_0, E_1] \,\&\, \mathrm{x_{tip}} - \mathrm{x} < 1 \text{ mm} \\ 0, \text{ otherwise} \end{cases}, \tag{6}$$

where Ψ is the volume of the numerical ionization zone, calculated in the simulation, it satisfies $|\mathbf{E}| \in [E_0, E_1] \,\&\, \mathrm{x_{tip}} - \mathrm{x} < 1$ mm ; I is the anode current, measured experimentally and used as a boundary condition in the numerical simulation. The condition $\mathrm{x_{tip}} - \mathrm{x}$ term limits the ion production along the needle. It is based on the experimental electrode setup – the tip extends 1 mm from the needle holder. $E_0 = 2.8 \times 10^6$ V/m is the critical field strength below which the number of ion recombination events is greater than the production per drift length for air [16]. $E_1 = 3.23 \times 10^6$ V/m is the breakdown electric field strength for air [1,9]. Since the charge density is balanced in the ionization region, the anode current equals the charge density flux at the ionization boundary.

B. Computational Domain and Conditions

The numerical model is implemented in a 2D axisymmetric simulation using a general purpose finite volume solver (ANSYS Fluent) [48]. A body force is added to the momentum equation; the ion motion is accounted for by the transport of charge density ρ_e, which is modeled as a user-defined scalar. The corona electrode is located on the axis of the domain, and the cathode ring is modeled as a semi-circle at the wall. Fig. 2 shows the schematic diagram of the geometry. The computational domain represents the geometry of the experimental apparatus. The inlet is located 10 mm upstream of the corona needle. The distance between the needle tip and the cathode ring is varied based on the experimental conditions. In the experiment, the needle tip has 1-micron radius of curvature as measured using optical microscopy; it is modeled as a point where the outer wall of the needle body intersects with the axis; these lines intersect at the angle of 1°. The geometry is gridded using ANSYS ICEM software [48].

The mesh is comprised of hexagonal cells; after conducting a mesh independence study, the number of cells was ~ 445,000. To balance mesh independence and convergence time, the average mesh size in the ionization and acceleration regions was ~ 266 μm/cell . Due to high drift velocities $|\mathbf{u}_{\text{charge}}| \sim O(100 m/s)$, the resolution of charge transport requires a time step $\Delta t = 10^{-7}$s to satisfy the CFL condition [49]:

$$\frac{|\mathbf{u}_{\text{charge}}|\Delta t}{\Delta x} \approx \frac{10^2 \times 10^{-7}}{10^{-5}} \leq O(1), \tag{7}$$

where $\mathbf{u}_{\text{charge}} = \mathbf{u} - \mu_b \nabla \varphi$ is the drift velocity of the ions. The simulations are initialized with zero values of pressure, velocity, and charge density. The air flow field and electric field develop spatiotemporally for the set boundary conditions. The steady-state flow is achieved when the outlet velocity profile is independent of the flow time; for most simulations, it is ~1s (10^7 time steps after initialization). Results are analyzed when steady-state conditions are reached.

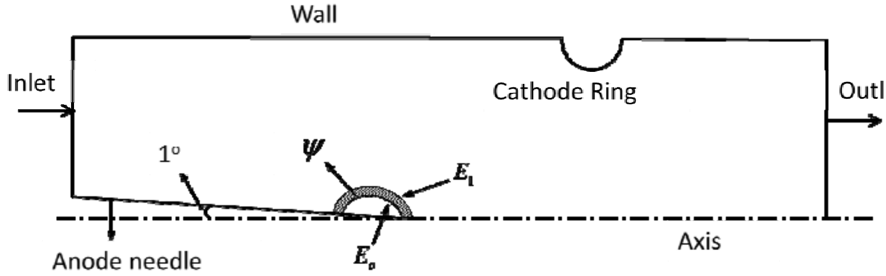

FIG. 2. The computational domain used for the numerical simulation; the model includes the ion generation region Ψ, defined by the thresholds of electric field values: E_0 and E_1 .

Table I summarizes the boundary conditions used in the numerical simulation. The air flow velocity is set to zero at the electrode surfaces and the tube wall due to the no-slip boundary condition. The inlet and outlet are set as atmospheric pressure boundaries. High voltage (4~10 kV) is applied to the anode needle, and zero voltage (grounded) is applied to the cathode ring. Zero electric potential gradient is applied to the other boundaries without solving the Eq. 4 within the isolated solid walls. The charge density is set to zero diffusive flux on wall boundaries, similar to previous modeling work [1,2,50,51]. In this Neumann boundary condition, the charge density at the boundary is extrapolated from the nearest cell.

The convective flux of charge density is resolved by the simulation, the ion drift velocity in an electric field is based on Eq. 3. The current flux at the cathode and the outlet (surface integral of the charge density flux) matches the input anode current, satisfying the conservation of current density (Kirchhoff's circuit law). The hyperbolic equations of NSE and charge density are resolved using the transient Semi-Implicit Method for Pressure-Linked Equations (SIMPLE) algorithm [52] with second-order discretization for both space and time. The electric field is resolved by the second order steady-state Poisson equation solver for every time step.

Table I. Boundary conditions for the numerical simulations.

Boundary	Conditions
Inlet pressure	Atmospheric pressure
Outlet pressure	Atmospheric pressure
Anode corona needle	4~11kV & Zero diffusive flux for charge
Cathode ring	0kV & Zero diffusive flux for charge
Wall boundaries	Zero gradients for electric potential & Zero diffusive or convection flux for charge
Anode current	Based on the experimental measurement

IV. RESULT AND DISCUSSION

A. Numerical Simulations

The numerical model represents the process by which the ion-molecule collisions accelerate the bulk air flow. FIG. 3 (left) shows the electric field lines between the corona electrode and the ground electrode. The greatest field strength is near the tip of the corona electrode with a small radius of curvature where the field intensity reaches the threshold for ion generation. The effect of the space charge on the electric field is apparent near the ionization region where the ion concentration is highest. This field line divergence is greater for higher voltages. The electric field distortion is less significant further away from the electrode tip since the charge density decays proportionally to $r^{3/2}$ [32,53]. In the $L = 7\ \mathrm{mm}$ case, the field lines are better aligned with the direction of the bulk flow leading to higher energy conversion efficiency, as discussed later in the manuscript. FIG. 3 (middle) shows the ion concentration contours. The ions are generated at the needle tip, and their motion is dominated by the electric field due to their very high electrical mobility, as the ion drift velocity at about two orders of magnitude greater than the average velocity of the bulk flow. The ions do not drift upstream significantly; some negative axial drift at the needle tip is observed due to the space charge effect for higher voltage cases, resulting in ions' negative work and reduction in the energy conversion. An annular recirculation flow pattern is formed upstream of the cathode ring near the wall. This is due to the adverse pressure gradient in the near wall acceleration region driven by the high electric field values at the ring electrode, as seen in FIG. 3 (left).

In the region downstream of the ground electrode, the electric field is weak and some ions exit the domain due to the relatively high flow velocities and the space charge effect (both are the highest at the centerline). The average values of the ion concentration at the device outlet are in the range of 1.7×10^{8} ions/cm^{3} (7 mm 7 kV) to 3.1×10^{8} ions/cm^{3} (3 mm 8 kV). These values are of the same order of magnitude as the experimental measurement $\sim 0.6\times10^{8}$ ions/cm^{3} (3 mm 7 kV), measured 25 mm downstream of the exit. The discrepancy is likely due to the ion dispersion after the flow exits the EHD flow chamber. The ion concentration at the outlet is highest at the axis because: (i) the centerline has the highest velocity, convecting ions from the domain, and (ii) the electric field lines near the wall downstream of the ground electrode are pointing in the reverse direction of the bulk flow, resulting in reverse ion drift. The maximum value of the electric field strength is 1.6×10^{8} V/m and the ion concentration is 1.0×10^{12} ions/cm^{3}, both near the needle tip region of the 3 mm 7 kV case. For better visualization, the values for the electric field and ion concentration contours in FIG. 3 are limited in range.

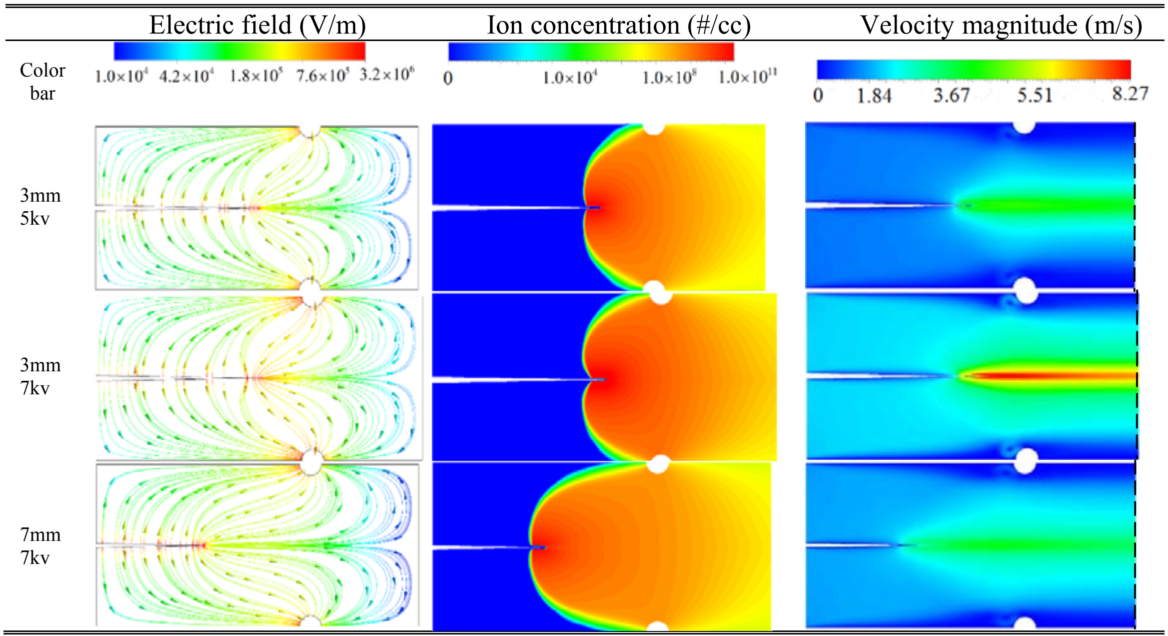

FIG. 3. Plots of the electric field, ion concentration, and velocity for different conditions in the point-to-ring corona generator ($I = 6.15\,\mu\text{A}, 16.04\,\mu\text{A}, 4.28\,\mu\text{A}$, respectively). The dash lines on the velocity contours indicate the location at which the velocity of the EHD flow is compared with the experiments.

B. Corona Currents

In previous work, the charge density input in the simulation is "tuned" to match the cathode current measured experimentally using an iterative approach [1-5,35-41]. In this work, we directly compute the cathode current based on the boundary conditions; the numerical model uses corona voltage and anode current as input parameters. The comparison of cathode current from the simulation and the experimental values is used for model validation. The cathode current is calculated by integrating the charge density flux on the ground electrode surface:

$$I_{\text{cathode}} = \int_{\substack{\text{cathode}\\\text{surface}}} -\mu_b \rho_e \nabla \varphi \, d\mathbf{A}_{\text{cathode}} \,, \tag{8}$$

where $\mathbf{A}_{\text{cathode}}$ is the area vector of the cathode. Table II shows the comparison between the experimentally measured and computed anode and cathode current. The cathode current in the simulation agrees within 5% with the experimental measurements. The cathode recovers 85~90% of the ion current generated by the corona electrode. The 10~15% current reduction is associated with ions exiting the domain.

Table II. Comparison of cathode current between the experiments and CFD.

	Anode Current (μA)	Experimental Cathode Current (μA)	CFD Cathode Current (μA)
3mm, 5kV	6.15	5.23	4.99
3mm, 7kV	16.04	14.42	14.21
7mm, 7kV	4.28	3.82	3.64

C. Maximum Velocity and Velocity Radial Distribution

To further validate the numerical model, we compare the exit velocities from the experimental data, the analytical solution by Guan et al. [32,53], and the numerical result (FIG. 4) for the $L = 3\,\mathrm{mm} \sim 7\,\mathrm{mm}$ cases and corona voltages of $\varphi = 4 \sim 10\,\mathrm{kV}$. The experiments and simulations show the maximum velocities are on the centerline at the outlet. FIG. 4 shows the comparison. The numerical model agrees within 5% error with the experimental data and the analytical predictions. The analytical predictions are generally higher than the numerical results since it does not account for viscous drag or the non-unidirectional flow. For a given point-to-ring distance, the maximum outlet velocity increases linearly with corona voltage. This linear trend of maximum velocity was also observed by Zhang et al. in the external flow with point-to-ring corona configurations [15] and by Kim et al. for the planar electric field ion generator [54]. For a given corona voltage, the maximum velocity increases as L decreases, due to a stronger electric field. The maximum corona voltage, however, is limited by the device glow-to-arc transition limit [16]. When arc discharge happens (in our case: 9 kV for L = 3 mm, 10 kV for L = 5 mm, 11 kV for L = 7 mm), the flow velocity reduces to zero. The maximum EHD induced air flow was 9.0 m/s (3 mm 8 kV) from both the experiments and simulations.

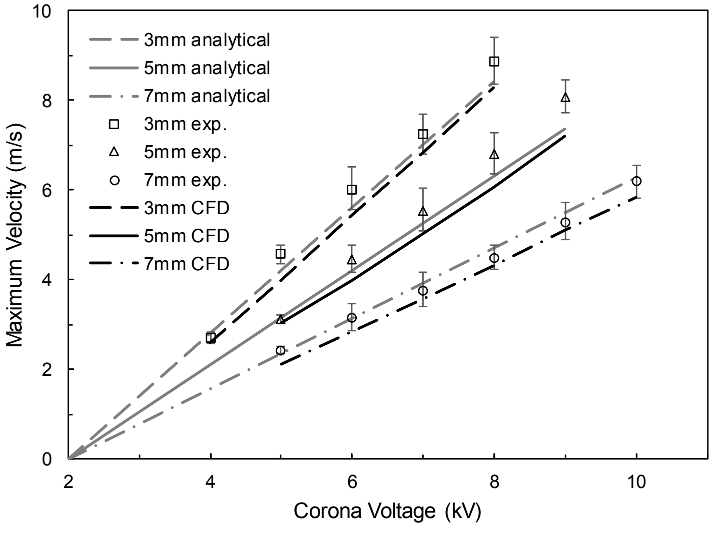

FIG. 4. Maximum velocity as a function of corona voltage and electrode geometry for the experimental data, analytical [32,53], and CFD results.

D. Velocity Profiles

To study the spatial distribution of velocity, we compare the numerical and experimental velocity profiles at the outlet of the point-to-ring EHD flow generator. In Fig. 5 (a), the velocity profiles are plotted for two voltage values at a fixed electrode spacing (L = 3 mm). The higher voltage case produces higher velocities with very similar velocity profiles. Fig. 5 (b) shows that, at a fixed voltage, the velocity increases when L decreases. Both numerical and experimental results show a distinct peak at the axis, consistent with the results in FIG. 3. The velocity profiles then decay rapidly with radial distance. Numerical and experimental results agree within 5% error at the centerline, but the model is less accurate at the edges of the domain. The discrepancy in this region may be due to flow instability in the shear flow region that modifies the radial location of the inflection points in the velocity profile.

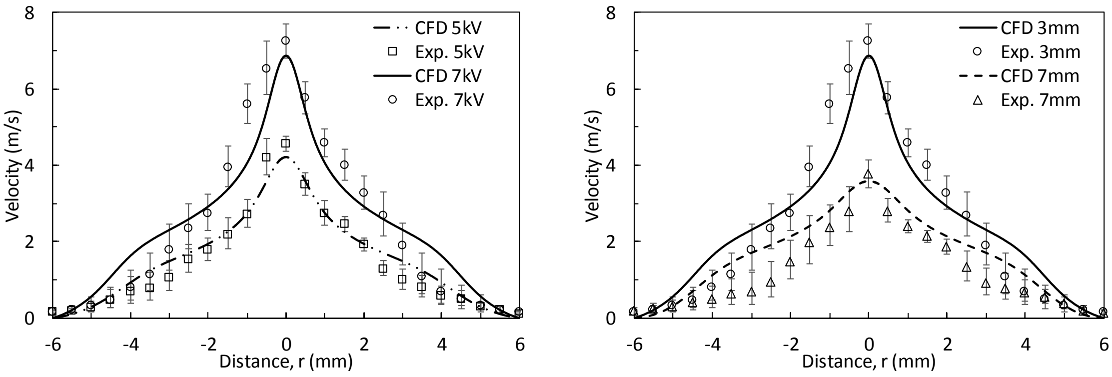

(a) (b)

FIG. 5. Comparison between simulations and experiments for the velocity profiles at the outlet of the EHD generator; (a) varying corona voltages at a fixed distance, and (b) varying anode-cathode distance (L) at a fixed corona voltage.

The velocity profile shows that the EHD-induced airflow in a point-to-ring corona discharge has parallels to a submerged jet [55]. For submerged jets, the Reynolds number is determined based on the nozzle diameter and the mean velocity at the exit [56]. In the case of corona discharge flow, the nozzle is replaced by the EHD jet located at the centerline, immediately downstream of the corona electrode tip. The Reynolds number (Re) in the EHD flow is ~ 700-900, based on the diameter of the jet, for L = 3 mm, 7 kV, d_{jet} ~ 2-3 mm, and mean velocity u ~ 4-5.5 m/s. Other cases have smaller Re due to lower jet velocities, except for the 3 mm, 8 kV case, where Re is still < 1000 (~ 6.5 m/s in mean velocity and d_{jet} ~ 2-3 mm). Therefore, the EHD flow can be represented by a fully laminar jet ($300 < \mathrm{Re} < 1000$) [56].

E. Non-Dimensional Analysis

The simulation shows that the EHD force drives local flow accelerations. The global parameters used in the analytical model and ones reported in the literature for a description of the EHD flow do not account for spatial distributions in ρ_e and φ. Further insight into the development of EHD flow in different regions of the geometry can be gained by non-dimensional analysis. The non-dimensional EHD equation can be written as:

$$\mathrm{St}\frac{\partial \mathbf{u}^*}{\partial t^*}+\left(\mathbf{u}^*\cdot\nabla^*\right)\mathbf{u}^*=-\nabla^* P^*+\frac{1}{\mathrm{Fr}^2}\mathbf{g}^*+\frac{1}{\mathrm{Re}}\nabla^{*2}\mathbf{u}^*-\left[\frac{\rho_e\varphi}{\rho\mathbf{u}^2}\right]\rho_e^*\nabla^*\varphi^*, \quad (9)$$

where St is the Strouhal number, Fr is the Froude number, the superscript * denotes non-dimensional variables [57]. A proposed non-dimensional parameter, $\mathrm{X}=\rho_e\varphi/\rho\mathbf{u}^2$, is defined as the ratio of electrostatic to inertial terms. In global terms, the parameter X is related to the electro-inertial number $\mathrm{N}_{\mathrm{EI}}=\varepsilon\left|\vec{E}\right|^2/\rho\mathbf{u}^2$ [58], described in the literature as $\mathrm{Md}/\mathrm{Re}^2$, where $|\mathbf{E}|$ is the magnitude of the electric field vector, and Md is the Masuda number [59]. The parallels come from the electric description based on Gauss' law. Gauss' law can be written in a non-dimensional form as:

$$\frac{\varphi}{L^2}\nabla^{*2}\varphi^* = -\frac{\rho_e}{\varepsilon} \tag{10}$$

$$\frac{\varphi}{L}\nabla^{*}\varphi^* = -|\mathbf{E}|\ . \tag{11}$$

Since $\nabla^{*2}\varphi^*$ and $\nabla^*\varphi^*$ are non-dimensional parameters, re-arranging the Eq. 10 and Eq. 11 gives:

$$\varepsilon|\mathbf{E}|^2 = \rho_e\varphi, \tag{12}$$

where the dimension of both terms in Eq. 12 is the same. The main difference is that the parameter X can be resolved spatially. Non-dimensional analysis of the EHD system that does not include the spatial inhomogeneity of ρ_e and φ fails to describe the local effects of electrostatic force on the flow because Md and $\mathrm{N_{EI}}$ can only be used as global parameters. To gain insight into corona-driven EHD flow, the electric force and flow inertial and viscous terms have to be resolved spatially. The non-dimensional parameter, X, can be computed directly from the governing equations for each region of the flow, providing the relative contribution of the terms locally. Cotton et al. suggests that, when the electro-inertial number is greater than unity, the flow is dominated by the EHD force [60]. Though the analysis is valid as an order of magnitude estimation of the system, in our modeling, the use of the conventional N_{EI} formulation led to over-estimating the effect of EHD in regions with low charge density and strong electric field, such as the region upstream of the corona electrode tip (shown in the supplementary materials). In this region, the ions – molecule collision cannot drive the flow since their concentration of ions is too low. FIG. 6 shows electric field lines colored by the values of X, indicating the regions where the electric force is higher than the inertial force. The EHD-dominated flow (red) is located between the corona and ground electrode where both the ion concentration and the electric field strength are high (see FIG. 3). In the 7 mm case, the red colored vectors are well aligned with the flow direction, which results in a higher energy transfer efficiency than in the 3 mm cases (FIG. 7). There exists another EHD-dominated region located at the edge of the domain where the electric lines are pointing in the opposite direction of the main flow; the inertial flow component in this region is very small. The small denominator in the calculation of parameter X results in its high values (up to 400). The negative electric force, combined with the high viscous stress, explain the low-velocity region at the edge of the domain (see FIG. 5).

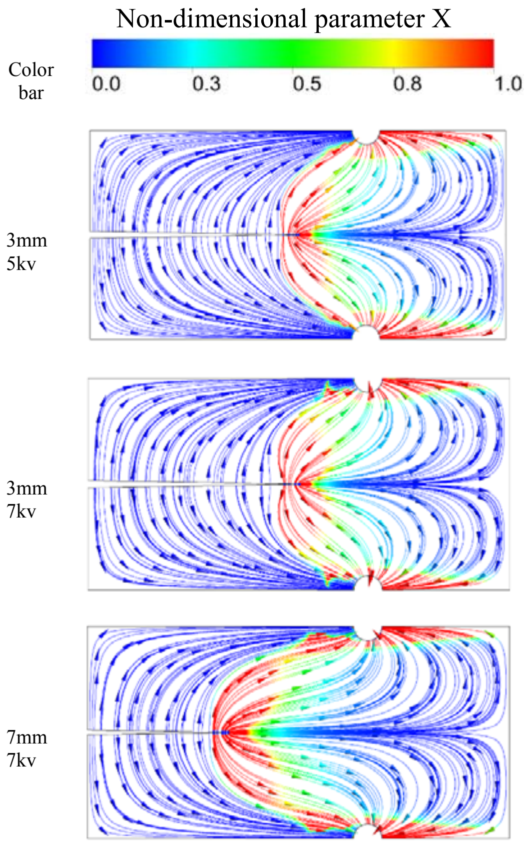

FIG. 6. Electric field lines colored by the non-dimensional parameter X. The red zone, $X \geq 1$, indicates the regions of EHD-dominated flow. The color map is limited to $X = 1$; the value X can be as high as 400 in the regions near the ionization zone and the low-velocity region near the wall.

F. Energy Transfer Efficiency

The energy conversion efficiency can be calculated from the ratio of the kinetic energy flux in the flow at the exit of the EHD device to the electrical power produced by the corona discharge.

$$\eta = \frac{\frac{1}{2}\rho\int u^3 dA}{\varphi I}. \tag{13}$$

The corona voltage and anode current are obtained from the experiments. The kinetic energy flux in the flow is calculated from both the experimental and numerical velocity profiles. Table III shows the values used in the calculation of energy transfer efficiency.

Table III. Comparison of electrical and fluid power between the experiments and the CFD.

	3 mm, 5 kV	3 mm, 7 kV	7 mm, 7 kV
$W_{K,Exp}(mW)$	$0.196 \pm 16\%$	$0.882 \pm 19\%$	$0.264 \pm 23\%$
$W_{K,CFD}(mW)$	0.184	0.86	0.293
$I(\mu A)$	6.15	16.04	4.28
$W_E(mW)$	30.8	112.28	29.96

Energy transfer efficiency is shown in FIG. 7. The numerical results agree well with the efficiency computed using the experimental data. Efficiency is higher in the 7 mm cases than in the 3 mm cases due to the smaller angle between the axial velocity and the electric field vectors, as is shown FIG. 6. Energy transfer efficiency peaks at a certain corona voltage (7 kV for 3 mm, and 8 kV for 7 mm) after which the efficiency decreases. This nonlinear effect is likely due to the quadratic relationship between the corona voltage and anode current. The increase in corona voltage results in a quadratic increase in the anode current and a cubic increase in the electric power $\varphi I \propto \varphi^3$. Maximum velocity at the centerline is linearly proportional to the corona voltage based on the analytical solution and previously reported experimental observations, but the kinetic power $\frac{1}{2}\rho\int u^3 dA$ is not proportional to φ^3 because u is not proportional to φ anywhere but on the centerline. At the high values of the corona voltage, the field lines also diverge due to the high space at the corona needle (see FIG. 3 and FIG. 6) resulting in a negative work of the electric field.

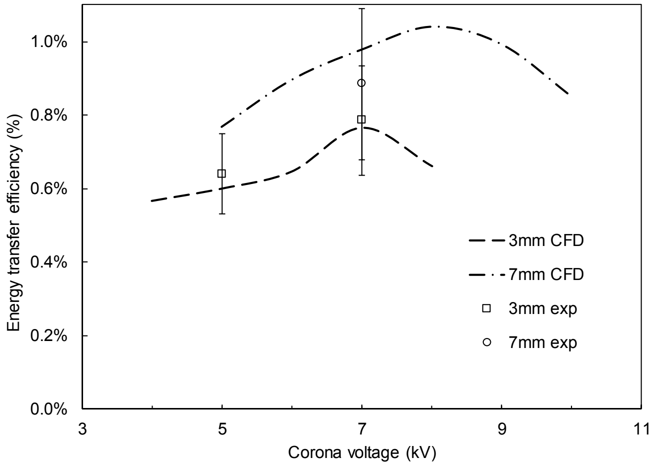

FIG. 7. Energy transfer efficiency from the experiments (symbols) and simulations (dashed and dash-dotted lines).

V. CONCLUSION AND FUTURE WORK

This work presents an experimental and numerical investigation of corona discharge-driven flow. The experimental data for flow in the point–to-ring internal geometry includes voltage, current, and velocity profile measurements. The numerical approach accounts for the electric force exerted by the ions on the neutral gas; this body force is added to the Navier-Stokes equations. The addition of the volumetric charge flux into the numerical ionization zone allows for the direct simulation of the corona-driven EHD flow. The model uses the measured corona voltage and anode current as inputs to resolve the velocity and electric fields and the charge density. Local balances of electric and inertial terms are used to determine a non-dimensional parameter X, which has similarity to the electro-inertial number N_{EI} [58]. As the global criteria, $N_{EI} > 1$, indicates the presence of the secondary EHD flows [60], the local criteria, $X \geq 1$, sheds insight on the relationship between the electric body force and inertial flow and determines the flow dominated by the electric field, inertia, or viscous effects. The numerical model is validated using axisymmetric simulations compared against the experimental data for point-to-ring corona-driven EHD flow; the cathode current and the outlet velocity profile from the simulation agree within 5% error of the experimental data. The maximum velocity is directly proportional to the corona voltage, consistent with previous results [15]. Unlike in canonical internal pipe flow, the velocity profile in the point-to-ring EDH flow is analogous to a submerged jet [55], for which the Re is determined by the dimension of the acceleration zone and mean velocity. Jet values of $\mathrm{Re} = 300 - 1000$ correspond to the laminar regime in the flow acceleration region [56].

The model takes into account the effect of viscous stresses near the walls, as well as the balance between inertia and electric forces; it captures the experimental velocity profile better than the analytical model that only provides accurate predictions near the centerline. The exit velocity profile is used to calculate the electric to kinetic energy transfer efficiency. The efficiency is highest when the point-to-ring distance is largest, due to a smaller angle between the electric field gradient and the flow direction and to the lower viscous losses. The efficiency peaks at intermediate corona voltages, for a given electrode distance, due to the quadratic current-voltage relation and the nonlinear decrease of velocity away from the centerline, as well as the field line distortions caused by space charge effect near the ionization region.

VI. ACKNOWLEDGEMENTS

This research was supported by the DHS Science and Technology Directorate, Homeland Security 530 Advanced Research Projects Agency, Explosives Division and UK Home Office; grant no. HSHQDC-15-531 C-B0033, by the National Institutes of Health, grant NIBIB U01 EB021923.

This manuscript is based on the Ph.D. research of Mr. Guan, who has developed the analytical and numerical models and has provided major contributions to the manuscript preparation. Mr. Vaddi is responsible for performing the experiments and analysis of the experimental data. Prof. Aliseda provided expertise in the experimental measurement of the velocity profiles, advice in data interpretation and manuscript preparation. Prof. Novosselov is the academic advisor for Guan and Vaddi and is responsible for the overall direction of the project and has provided day-to-day guidance in the experimental and modeling work, data analysis, and manuscript preparation.

VII. REFERENCES

[1] N. Jewell-Larsen, P. Zhang, C.-P. Hsu, I. Krichtafovitch, and A. Mamishev, Coupled-physics modeling of electrostatic fluid accelerators for forced convection cooling, in *9th AIAA/ASME Joint Thermophysics and Heat Transfer Conference*, 2006, p. 3607.

[2] D. B. Go, S. V. Garimella, and T. S. Fisher, Numerical simulation of microscale ionic wind for local cooling enhancement, in *Thermal and Thermomechanical Phenomena in Electronics Systems, 2006. ITHERM'06. The Tenth Intersociety Conference on* IEEE, 2006, pp. 45.

[3] D. B. Go, S. V. Garimella, T. S. Fisher, and R. K. Mongia, Ionic winds for locally enhanced cooling, Journal of Applied Physics **102**, 053302 (2007).

[4] D. B. Go, R. A. Maturana, T. S. Fisher, and S. V. Garimella, Enhancement of external forced convection by ionic wind, International Journal of Heat and Mass Transfer **51**, 6047 (2008).

[5] N. Jewell-Larsen, C. Hsu, I. Krichtafovitch, S. Montgomery, J. Dibene, and A. V. Mamishev, CFD analysis of electrostatic fluid accelerators for forced convection cooling, IEEE Transactions on Dielectrics and Electrical Insulation **15** (2008).

[6] O. M. Stuetzer, Ion drag pressure generation, Journal of Applied Physics **30**, 984 (1959).

[7] I. Krichtafovitch, V. Gorobets, S. Karpov, and A. Mamishev, Electrostatic fluid accelerator and air purifier–The second wind, in *Annual Meeting of the Electrostatics Society of America*, 2005, pp. 1.

[8] N. Jewell-Larsen, D. Parker, I. Krichtafovitch, and A. Mamishev, Numerical simulation and optimization of electrostatic air pumps, in *Electrical Insulation and Dielectric Phenomena, 2004. CEIDP'04. 2004 Annual Report Conference on* IEEE, 2004, pp. 106.

[9] T.-Y. Wen, T.-T. Shen, H.-C. Wang, and A. Mamishev, Optimization of wire-rod electrostatic fluid accelerators, in *Electronic Components and Technology Conference (ECTC), 2013 IEEE 63rd* IEEE, 2013, pp. 240.

[10] Y. Ju and W. Sun, Plasma assisted combustion: Dynamics and chemistry, Progress in Energy and Combustion Science **48**, 21 (2015).

[11] E. Moreau, Airflow control by non-thermal plasma actuators, Journal of physics D: applied physics **40**, 605 (2007).

[12] K.-S. Choi, T. Jukes, and R. Whalley, Turbulent boundary-layer control with plasma actuators, Philosophical Transactions of the Royal Society of London A: Mathematical, Physical and Engineering Sciences **369**, 1443 (2011).

[13] L. Y. Yeo, D. Hou, S. Maheshswari, and H.-C. Chang, Electrohydrodynamic surface microvortices for mixing and particle trapping, Applied physics letters **88**, 233512 (2006).

[14] E. Moreau, N. Benard, J.-D. Lan-Sun-Luk, and J.-P. Chabriat, Electrohydrodynamic force produced by a wire-to-cylinder dc corona discharge in air at atmospheric pressure, Journal of Physics D: Applied Physics **46**, 475204 (2013).

[15] Y. Zhang, L. Liu, Y. Chen, and J. Ouyang, Characteristics of ionic wind in needle-to-ring corona discharge, Journal of Electrostatics **74**, 15 (2015).

[16] E. E. Kunhardt and L. H. Luessen, Electrical Breakdown and Discharges in Gases-Part B, Macroscopic Processes and Discharges, Eds. EE Kunhardt and LH Luessen, Plenum, NY (1981).

[17] S. Mukkavilli, C. Lee, K. Varghese, and L. Tavlarides, Modeling of the electrostatic corona discharge reactor, IEEE transactions on plasma science **16**, 652 (1988).

[18] J.-S. Chang, P. A. Lawless, and T. Yamamoto, Corona discharge processes, IEEE Transactions on plasma science **19**, 1152 (1991).

[19] J. S. Townsend, XI. The potentials required to maintain currents between coaxial cylinders, The London, Edinburgh, and Dublin Philosophical Magazine and Journal of Science **28**, 83 (1914).

[20] J. S. Townsend, *Electricity in gases* (Рипол Классик, 1915).

[21] R. Sigmond, Simple approximate treatment of unipolar space‐charge‐dominated coronas: The Warburg law and the saturation current, Journal of Applied Physics **53**, 891 (1982).

[22] K. Yamada, An empirical formula for negative corona discharge current in point-grid electrode geometry, Journal of applied physics **96**, 2472 (2004).

[23] S. I. Wais and D. D. Giliyana, Sphere-to-plane electrodes configuration of positive and negative plasma corona discharge, Am J Mod Phys **2**, 46 (2013).

[24] P. Mikropoulos and V. Zagkanas, A computational method for positive corona inception in the coaxial cylindrical electrode arrangement in air under variable atmospheric conditions, in *Proceeding of the 16 th International Symposium on High Voltage Engineering. Paper B-10*, 2009.

[25] Y. Zheng, B. Zhang, and J. He, Current-voltage characteristics of dc corona discharges in air between coaxial cylinders, Physics of Plasmas **22**, 023501 (2015).

[26] A. A. Martins, Simulation of a wire-cylinder-plate positive corona discharge in nitrogen gas at atmospheric pressure, Physics of Plasmas **19**, 063502 (2012).

[27] P. Giubbilini, The current‐voltage characteristics of point‐to‐ring corona, Journal of applied physics **64**, 3730 (1988).
[28] P. Giubbilini, Mobility measurement of large ions in air from a point-to-ring corona source, Journal of applied physics **81**, 2101 (1997).
[29] V. T. Dau, T. X. Dinh, T. T. Bui, C.-D. Tran, H. T. Phan, and T. Terebessy, Corona based air-flow using parallel discharge electrodes, Experimental Thermal and Fluid Science **79**, 52 (2016).
[30] M. J. Johnson, R. Tirumala, and D. B. Go, Analysis of geometric scaling of miniature, multi-electrode assisted corona discharges for ionic wind generation, Journal of Electrostatics **74**, 8 (2015).
[31] R. Tirumala and D. B. Go, Comparative study of corona discharge simulation techniques for electrode configurations inducing non-uniform electric fields, Journal of Electrostatics **72**, 99 (2014).
[32] Y. Guan, R. S. Vaddi, A. Aliseda, and I. Novosselov, Electro-hydrodynamic Flow in Point-to-Ring Corona Discharge, Physical Review Fluids(submitted) (2017).
[33] L. N. Trefethen and t. C. d. team, Chebfun version 4.2, 2011.
[34] T. A. Driscoll, N. Hale, and L. N. Trefethen, Chebfun guide, Pafnuty Publications, Oxford, 2014.
[35] K. Adamiak and P. Atten, Simulation of corona discharge in point–plane configuration, Journal of electrostatics **61**, 85 (2004).
[36] L. Zhao and K. Adamiak, EHD flow in air produced by electric corona discharge in pin–plate configuration, Journal of electrostatics **63**, 337 (2005).
[37] L. Zhao and K. Adamiak, Numerical simulation of the effect of EHD flow on corona discharge in compressed air, IEEE Transactions on Industry Applications **49**, 298 (2013).
[38] P. Lawless and L. Sparks, Interactive computer model for calculating VI curves in ESPs (electrostatic precipitators): Version 1. 0. Report for July 1984-July 1986, 1986.
[39] S. Cristina, G. Dinelli, and M. Feliziani, Numerical computation of corona space charge and VI characteristic in DC electrostatic precipitators, IEEE Transactions on industry applications **27**, 147 (1991).
[40] T. Yamamoto, M. Okuda, and M. Okubo, Three-dimensional ionic wind and electrohydrodynamics of tuft/point corona electrostatic precipitator, IEEE Transactions on Industry Applications **39**, 1602 (2003).
[41] K. Adamiak, Numerical models in simulating wire-plate electrostatic precipitators: A review, Journal of Electrostatics **71**, 673 (2013).
[42] N. A. Kaptsov, Electrical phenomena in gases and vacuum, Gostehizdat, Moscow, 1950.
[43] F. Peek, The law of corona and the dielectric strength of air, Proceedings of the American Institute of Electrical Engineers **30**, 1485 (1911).
[44] Y.-s. Cheng, H.-C. Yeh, and G. M. Kanapilly, Collection efficiencies of a point-to-plane electrostatic precipitator, The American Industrial Hygiene Association Journal **42**, 605 (1981).
[45] P. Stainback and K. Nagabushana, Review of hot-wire anemometry techniques and the range of their applicability for various flows, Electronic Journal of Fluids Engineering **1**, 4 (1993).
[46] J. Chen and J. H. Davidson, Model of the negative DC corona plasma: comparison to the positive DC corona plasma, Plasma chemistry and plasma processing **23**, 83 (2003).
[47] L. Hector and H. Schultz, The dielectric constant of air at radiofrequencies, Physics **7**, 133 (1936).
[48] ANSYS, v17.0, 2017.

[49] R. J. LeVeque, *Finite volume methods for hyperbolic problems* (Cambridge university press, 2002), Vol. 31.
[50] D. Cagnoni, F. Agostini, T. Christen, N. Parolini, I. Stevanović, and C. De Falco, Multiphysics simulation of corona discharge induced ionic wind, Journal of Applied Physics **114**, 233301 (2013).
[51] K. Luo, J. Wu, H.-L. Yi, and H.-P. Tan, Lattice Boltzmann model for Coulomb-driven flows in dielectric liquids, Physical Review E **93**, 023309 (2016).
[52] H. K. Versteeg and W. Malalasekera, *An introduction to computational fluid dynamics: the finite volume method* (Pearson Education, 2007).
[53] Y. Guan, R. S. Vaddi, A. Aliseda, and I. Novosselov, Supplemental information for Experimental and Numerical Investigation of Electro-Hydrodynamic Flow in a Point-to-Ring Corona Discharge Physical Review Fluids(submitted) (2017).
[54] C. Kim, D. Park, K. Noh, and J. Hwang, Velocity and energy conversion efficiency characteristics of ionic wind generator in a multistage configuration, Journal of Electrostatics **68**, 36 (2010).
[55] L. D. Landau, E. M. Lifshitz, J. B. Sykes, and W. H. Reid, *Fluid Mechanics* (Pergamon press inc, 1959), Course of theoretical physics, 6.
[56] K. McNaughton and C. Sinclair, Submerged jets in short cylindrical flow vessels, Journal of Fluid Mechanics **25**, 367 (1966).
[57] P. K. Kundu, I. M. Cohen, and D. Dowling, *Fluid Mechanics 4th* (ELSEVIER, Oxford, 2008).
[58] J.-S. Chang, A. J. Kelly, and J. M. Crowley, *Handbook of electrostatic processes* (CRC Press, 1995).
[59] IEEE-DEIS-EHD-Technical-Committee, Recommended international standard for dimensionless parameters used in electrohydrodynamics, IEEE Transactions on Dielectrics and Electrical Insulation **10**, 3 (2003).
[60] J. Cotton, A. Robinson, M. Shoukri, and J. Chang, A two-phase flow pattern map for annular channels under a DC applied voltage and the application to electrohydrodynamic convective boiling analysis, International Journal of Heat and Mass Transfer **48**, 5563 (2005).